Nanocalorimetry for Plasma Metrology Relevant to Semiconductor Fabrication

Running title: Nanocalorimetry for Plasma Metrology Relevant to Semiconductor Fabrication

Running Authors: Diulus et al.

J. Trey Diulus [1], Carles Corbella [2,3], Feng Yi [4], David LaVan [4], Berc Kalanyan [5], Mark McLean [4], Lakshmi Ravi Narayan [2,3], William A. Osborn [4], James E. Maslar [5], and Andrei Kolmakov [1,a)]

[1]Nanoscale Device Characterization Division, PML, NIST, Gaithersburg, MD 20899, USA
[2]PREP Associate, Materials Measurement Science Division, MML, NIST, Gaithersburg, MD 20899, USA
[3]Dept. Chemistry & Biochemistry, University of Maryland, College Park, MD 20742, USA
[4]Materials Measurement Science Division, MML, NIST, Gaithersburg, MD 20899, USA
[5]Chemical Sciences Division, MML, NIST, Gaithersburg, MD 20899, USA

[a)] Email: andrei.kolmakov@nist.gov

This letter reports on pilot tests of microfabricated nanocalorimeters as a metrology platform for rapid (< 40 ms response time) and sensitive (in the range of 10^{20} $m^{-2}s^{-1}$, 10^{17} m^{-3} for radicals' flux and density correspondingly) detection of neutral radicals generated by reactive cold plasmas. The setup consists of a nanocalorimeter resistive sensor coated with catalyst alongside an inert reference sensor with identical thermal masses. By measuring the temperature increase of the active sensor caused by radical surface recombination reactions and comparing it to the reference sensor, parasitic stimuli such as IR/visible/UV irradiation and ion- and/or electron-induced heat fluxes can effectively be isolated. The system was successfully tested in a hydrogen plasma environment, and critical performance metrics such as sensitivity and response time were evaluated and benchmarked against existing plasma radicals diagnostic techniques.

I. INTRODUCTION

Plasma-generated radicals are widely utilized in the semiconductor fabrication industry, for example, during dry etching, wafer cleaning, plasma-enhanced chemical/physical vapor deposition, in extreme ultraviolet lithography machines, etc. (see recent reviews [1, 2] and references therein). As the technology node size is further reduced, faster and finer control of plasma radical fluxes is required.[3, 4] The current real-time monitoring of plasma radicals typically employs optical emission/absorption spectroscopies (OES/OAS)[5], laser-induced fluorescence (LIF)[6, 7], or mass spectrometry.[8] However, despite the power of the aforementioned diagnostic methods, simple inexpensive sensors are needed for sensitive monitoring of neutral plasma-generated reactive radicals, particularly at the sample level under remote plasma conditions where the application of sensitive optical emission spectroscopy or mass spectrometry can be hampered.[9]

In this regard, radicals-induced heat flux sensors and etch sensors are often used as alternatives. The etch sensors measure the radical flux by detecting the change of mass of the reactive layer, which is gradually etched away due to a reaction with plasma radicals and ions.[10, 11] Quartz crystal microbalance (QCM) mass sensor precoated with amorphous carbon is usually used as an active element in these sensors. To decouple the etching by neutral from ionized species, either electrostatic retarding field[12, 13] or geometric factor that sponsors ion neutralization have been proposed.[14]

Alternatively, calorimetric heat flow probes utilize the heat of reaction specific to plasma radical recombination at the probe surface[15, 16]. Typically, calorimetric probes are made of millimeter-sized thin metal (or metal-coated) pads where metal (or coating) is selected based on its recombination coefficient and/or heat of reaction for a particular plasma radical to maximize the temperature increase. Single[17] or differential thermocouples[18-20], thermopiles[21], or fiber optics-

based IR detectors[22] are typically used for temperature readout in these sensors. The density of reactive species or radicals in plasma, like hydrogen, oxygen, and nitrogen atoms, can be estimated using heat balance models considering known plasma (reactor) parameters and values of radical(s) recombination coefficient(s)[23].

Plasma calorimetry metrology has matured and successfully validated since its early studies.[24-26] Further size and, therefore, thermal mass reduction of metal plate calorimeters is becoming challenging due to unavoidable signal-to-noise reduction, thereby limiting the accuracy of metrology under scenarios where low flux (density) and high spatial and temporal resolution are required. These challenges can be solved via microfabrication of nanocalorimeter devices that usually consist of ca. 100 nm thin suspended silicon nitride (SiN_x) membrane with lithographically defined metallic (e.g., Pt) resistive structure that serves as a temperature sensor and heater. The small size/thermal mass, functionalization versatility, and low wafer-scale fabrication cost of nanocalorimeters enable their facile integration into any reactor chamber to meet many plasma process-specific requirements. These SiN_x membrane-based nanocalorimeters, initially designed for fast scanning calorimetry[27, 28,29] can, in principle, have lateral dimensions in the order of a few microns, operate in the MHz frequency range[30, 31], and have been proven to detect fast physical and chemical endo/exo-thermal surface processes with sensitivity on the order of nJ/K, including adsorption-desorption processes, phase transitions, surface/interfacial reactions, and chemical etching reactions[32-34]. Despite the broad scope of micro-(nano)calorimetry research, no reports, to the best of our knowledge, have been made on using microfabricated nanocalorimeters for plasma diagnostics or plasma-induced process monitoring.

In this letter, we report on pilot tests of a nanocalorimeter sensor with a catalytic layer exposed to a low-pressure cold hydrogen plasma to evaluate the feasibility of this new metrology

platform for plasma diagnostics. Standard plasma characterization with OES is conducted alongside nanocalorimetry measurements to estimate hydrogen atom density values using a simple heat balance model. Finally, the performance of this new sensor is compared with the previously reported radicals detectors.

II. EXPERIMENTAL

MEMS-based nanocalorimetry chips were developed at the National Institute of Science and Technology, and their applications and tests have been described elsewhere[33]. Fig. 1(a) shows a schematic design of the first-generation plasma neutral radials sensor used in this study. Nanocalorimetry sensor chips measuring ca 5 mm × 13 mm in size were fabricated on Si wafers of 500 μm thickness. A low-stress 100 nm-thick silicon nitride layer was grown on these wafers. Onto this, a Ta/Pt (10 nm/100 nm) metal strip stack was lithographically defined and deposited. It serves as the Joule heating element and the 4-probe resistance sensor to determine the membrane temperature during the experiment. The silicon wafer was then lithographically etched from behind to create free-standing (ca 2 mm x 7.25 mm) silicon nitride membranes that provide thermal isolation and reduced thermal mass to the active area of the Pt sensor. The resistance of the Pt strip as a function of temperature was calibrated using a pyrometer during Joule heating of these sensors, and this relationship was used to determine the temperature of the sample during plasma exposure experiments. The fabrication, calibration protocols, and typical use of these sensors are described in detail elsewhere[35].

For the catalytically active radical sensor, the SiN_x membrane is coated on the plasma-facing side (Fig. 1(a)) with a Ti (5 nm) / Al_2O_3 (40 nm) / Ti (5 nm) / Au (30 nm) stack (catalytic Au material on top). To retain the same thermal mass, the reference sensor has the same materials

but reversed in the stack: Ti (5 nm) / Au (30 nm) / Ti (5 nm) / Al_2O_3 (40 nm) with Al_2O_3 layer on top (inert material). The front side of both sensor membranes has a lithographically defined Ta/Pt (10 nm/100 nm) strip (500 µm wide) as a heater and resistive temperature sensor. The temperature of the nanocalorimeter was set within the 303 K to 313 K (30 °C to 40 °C) range and hydrogen pressure stabilized before plasma ignition and was continuously measured during plasma exposure with 10 ms sampling time. Two nanocalorimetry sensors were mounted approximately 10 mm apart on a printed circuit board inside an aluminum grounded enclosure with slits. Thus, only the membrane part with the sensors is exposed to the plasma (Fig. 1(a)).

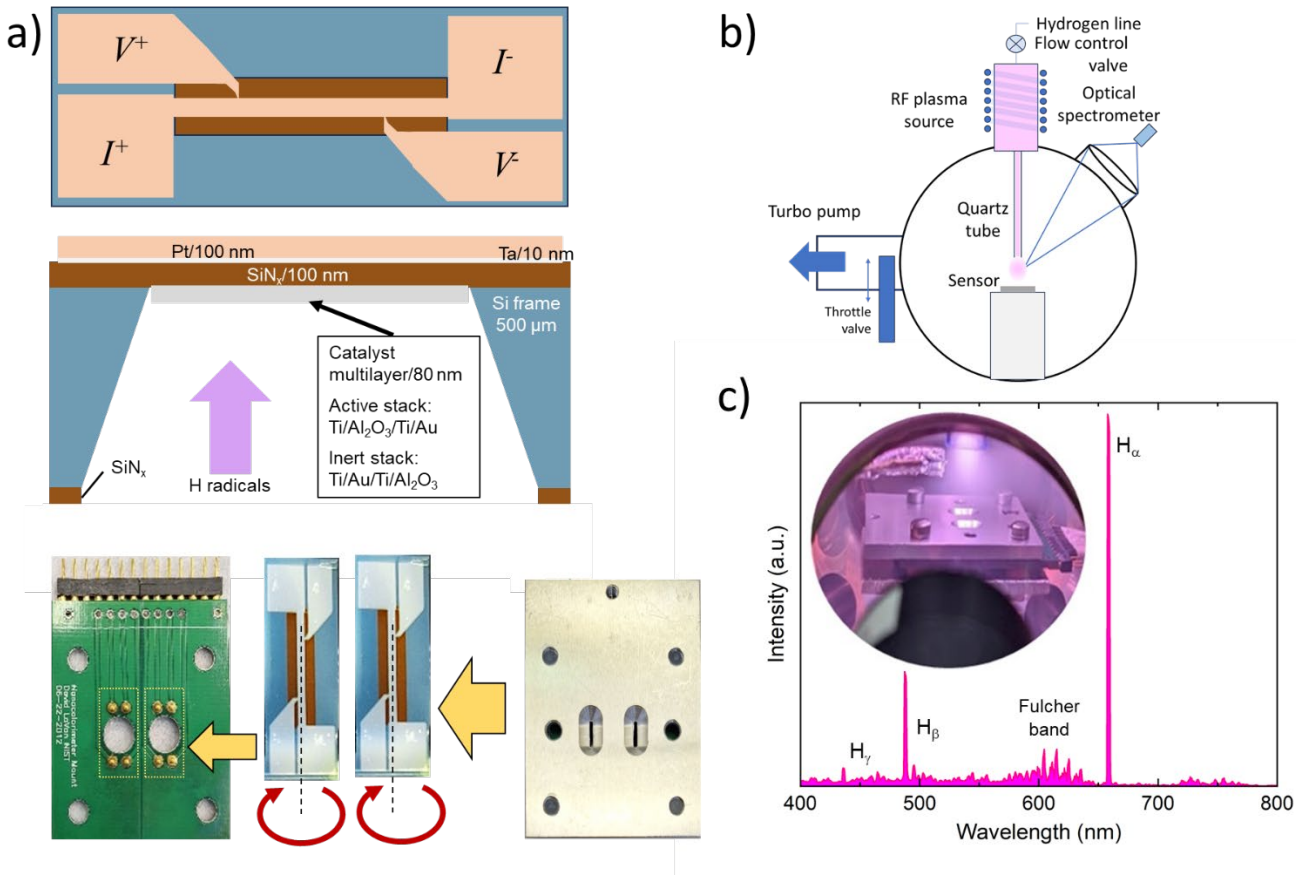

FIG. 1. (a) Schematic representations of top-view nanocalorimeter Pt heater strip and contacts (top), sensor side-view (middle), and enclosure hardware (bottom). The bottom section shows the assembly of two sensors whose placements on the circuit board are highlighted with dotted frames. Both sensors must be flipped around their dashed lines so that (1) Pt contacts face the Pogo Pins from the circuit board and (2) the catalyst multilayer is on the window side. Slit dimensions: 4.6 mm × 0.7 mm. (b) Experimental setup for plasma experiments. (c) Typical OES spectrum of a hydrogen plasma operated at 75 W, 13.56 MHz, 13 Pa. Inset: picture of plasma exposed sensor assembly taken from a viewport.

Plasma exposure experiments were performed in a high vacuum chamber pumped by an 80 L/s turbomolecular pump down to a base pressure of 10^{-5} Pa (Fig. 1(b)). Ultra-high purity hydrogen (99.999%) was delivered via a degassed stainless-steel gas line with an additional catalytic getter filter and microporous particulate filter to a commercial inductively coupled 75 W, 13.56 MHz plasma source. The pressure in the plasma source was set at 13 Pa or 26 Pa in this study using its automated feedback leak valve and the throttling gate valve in front of the turbopump. A quartz tube measuring 10 mm in inner diameter (12 mm outer diameter) and 158 mm in length was vacuum-tight connected to the discharge region of the plasma source and aimed at the nanocalorimeter sensors. This setup allows the variable positioning of the visible plasma plume above the sample surface to be regulated by the two aforementioned valves. Downstream remote plasma conditions with the visible edge of the glowing plume a few centimeters above the sensors were used in this study. The plasma plume itself was diagnosed via optical emission spectroscopy (OES) with a 185 nm to 1050 nm range and a 1.3 nm resolution spectrometer. Hydrogen emission spectra were collected through a quartz viewport and a collimating lens attached to the OES probe (Fig. 1(c)).

III. RESULTS AND DISCUSSION

The typical 26 Pa, 75 W plasma emission spectrum is depicted in Fig. 1(c). It is dominated by atomic hydrogen emission lines H_α (656.3 nm) and H_β (486.1 nm) from the Balmer series. Appreciable H_2 Fulcher molecular emission bands can also be observed and used to evaluate the degree of hydrogen dissociation in front of the sample. In particular, the ratio of densities of atomic versus molecular hydrogen, $[H]/[H_2]$, can be estimated by evaluating the intensities of the H_α line and (2-2) Q1 Fulcher transition from an excitation-deactivation model as described elsewhere[36]. Assuming an electron temperature within the range of 1-5 eV, usual in inductive discharges, and using the corresponding tabulated values of rate emission coefficients[37], a ratio interval $[H]/[H_2] \approx 0.1\text{-}0.5$ is obtained. Such a range of hydrogen radical ratios matches in order of magnitude with values measured in similar low-pressure hydrogen afterglows [15] and DC plasmas[38].

Fig. 2 (a) shows sensors' temperature versus time curves measured when the active (Au-coated) and "inert" reference (Al_2O_3-coated) nanocalorimeter sensors were exposed to downstream hydrogen 75 W, 13.56 MHz plasma at 26 Pa. The initial temperature of the sensors was set within the 296 K to 313 K range. The temperature variations upon ignition of the RF discharges measured in Au- and Al_2O_3-coated sensors are described as follows:

- *Gold-activated sensor*: Upon ignition onset, the sensor's temperature rises to around 409 K, with the measured response time ca. 40 ms (Fig.2 (b)) and reaches a maximum of around 415 K within a few seconds after that, presumably due to plasma source and sample surface stabilization. The small ripples observed just after ignition (see also insert in Figure 2b) are attributed to plasma-induced electronic noise, and their amplitude (ca 0.5 K) defines the current sensor sensitivity as discussed later. This temperature evolution occurs due to heat flux stabilization at the sensor, where heating due to plasma exposure and heat dissipation through

the leads on the chip (as well as through the holder) and thermal conductance through the gas eventually reaches equilibrium. Consistent with the reference sensor discussion below, and from multiple prior studies[26], the hydrogen atom exothermic recombination at the Au surface is a major factor for heating the sensor surface to the high temperature measured. After reaching the maximum, a gradual temperature decrease to a steady value of around 408 K is commonly registered. The slow monotonic decay of the sensor temperature to a constant value is ascribed to the poisoning of the Au catalyst by impurities desorbed from the chamber walls, which progressively contaminate the Au surface. Alternatively, variations in the gas composition of the discharge (e.g., $[H]/[H_2]$ ratio) due to plasma source temperature increase might also contribute to observed temperature decay. Upon plasma OFF onset with decay time ~ 70 ms, the temperature of the sensor drops to a value that is ca. 3 degrees higher compared to its initial value, which can be assigned to overall sensor chip heating during plasma

exposure. This initial δT temperature difference (Figure 2 a) decays within ca 10 s (not shown here).

- *Alumina-coated sensor*: In contrast with the behavior observed in the Au sensor, the temperature increase of the plasma-exposed alumina reference sensor is around only 8 degrees at the onset of plasma ignition. After that, a smooth but steady increase in temperature from the initial value to 316 K is observed until the discharge is extinguished. Such a drift can be explained by a consequence of progressive sensor heating due to the cumulative thermal effect of the incident plasma species: UV-vis-IR photons, ions, and electrons. Gradual surface activation because of plasma-assisted alumina reduction might also contribute to sensor heating[25]. Heating via hydrogen

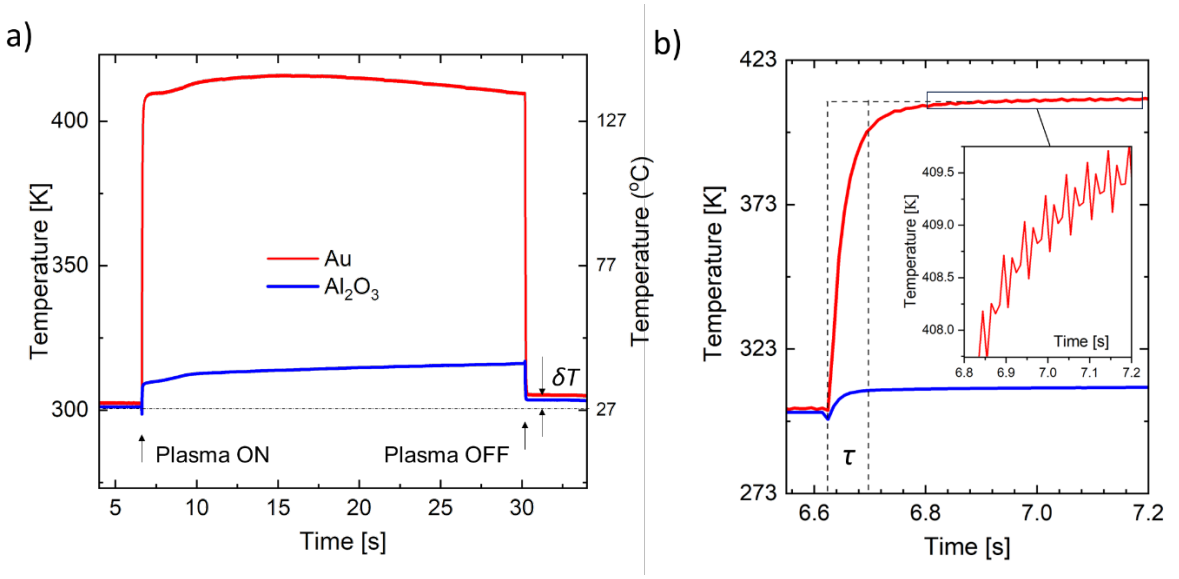

FIG. 2. (a) Temporal evolution of nanocalorimeter signals measured on Au and Al_2O_3 sensitized sensors upon plasma exposure at 26 Pa, 75 W, 13.56 MHz. Measurements using each sensor were performed in sequential experiments. $\boldsymbol{\delta T}$ denotes the sensor's temperature difference just before and after plasma exposure. (b) Zoomed-in plasma onset region. The rise time $\boldsymbol{\tau}$ is defined as a period between the plasma onset and when the temperature signal reaches 90 % of its saturation value. The 40 ms sensor response time, on the other hand, is defined here as the FWHM of the dT/dt. Insert: temperature noise level at steady state.

recombination is significantly reduced compared to the Au-activated sensor, which corroborates with an appreciably smaller recombination probability of hydrogen atoms on fully or partially oxidized aluminum.[20, 39, 40] Subtracting the alumina recombination coefficient from the Au one, the alumina reference sensor response can be used to quantitatively discriminate between the actual radical influx contribution to the Au sensor signal and all the rest of the plasma-induced heat fluxes.

The above data can be used to estimate the flux of hydrogen radicals j_H impinging onto the sensor(s), along with their corresponding density n, assuming $j_H = 0.25 \cdot n \cdot v$ (here $v = (8\kappa T/\pi m)^{1/2}$ is an average hydrogen velocity as per gas kinetic theory; T is the gas temperature in the vicinity of the sensor; κ is the Boltzmann constant ($1.4 \cdot 10^{-23}$ J/K), and m is the hydrogen atom mass ($1.7 \cdot 10^{-27}$ kg)) and by applying a simple heat balance model that considers heating of the sensor by the plasma and heat dissipation to the sensor holder and gaseous ambient. One can ignore radiative colling channel contribution in our temperature range. There are two heating channels generated by the plasma: (1) hydrogen radicals' recombination on the sensor surface $H + H \rightarrow H_2 + E_R$ (here E_R is a heat of recombination) and (2) VUV-IR photon irradiation together with electron- and ion-fluxes induced heating. Assuming that both Au- and alumina-activated sensors receive the same flux of radicals, photons, and charged particles from the plasma source and dissipate the heat equally, the radical heat flux contributions can be extracted by subtracting the measured Al_2O_3 (inert) signal from the Au-terminated sensor (active) reading and, additionally, considering their difference in hydrogen recombination coefficients. Thus, the heat flux (incoming power) due to hydrogen atom recombination, P_H, can be expressed as a function of j_H:

$$P_H = j_H \cdot A \cdot E_R \cdot \gamma \quad (1)$$

where A is the surface area of the suspended membrane coated with a catalyst layer (15 mm^2); E_R ≈ 4.5 eV - the dissociation energy of the H_2 molecule; γ is the difference between γ_{Au} and γ_{Al2O3} surface recombination coefficients. The latter parameter, however, scatters significantly in the literature due to different experimental conditions used.[14, 20, 39-42] Given that measured $\gamma_{Au} \gg \gamma_{Al2O3}$, we conservatively use the value $\gamma_{Au} - \gamma_{Al2O3} \sim 0.1$ in our estimations. In equilibrium, the incoming power equals heat dissipation (cooling power), $P_H = P_{cool}$, as suggested by Mozetic et al.[25], the cooling rate dT/dt right after the plasma is turned off:

$$P_{cool} = C_s \cdot dT/dt \quad (2)$$

Where C_s is the heat capacity of the sensor. Its estimation based on the material properties, surface area, and thickness provides a nominal value of 9×10^{-6} J/K, which roughly matches the heat capacity obtained from calibration measurements. The incident flux of atomic hydrogen onto the sensor surface can then be determined by isolating j_H from the equilibrium equation:

$$j_H = C_s(dT/dt) / (A \cdot E_D \cdot \gamma) \quad (3)$$

Hence, j_H takes the approximate value of $2 \cdot 10^{22}$ $m^{-2}s^{-1}$ for the hydrogen plasma at the explored pressures and geometry of the experiment. The latter corresponds to $n \approx 4 \cdot 10^{19}$ m^{-3} H-radicals density, which agrees in order of magnitude with values obtained for hydrogen discharges of similar power, pressure, and geometries reported elsewhere[30]. The estimated value of H radicals influx yields a corresponding partial pressure of H radicals around 0.07 Pa, which corresponds to [H]/[H_2] ratio of approximately 1 %. This number, however, is one order of magnitude lower compared to the above OES data collected at the edge of the glowing plume. Such discrepancy is expected since only a fraction of reactive species can reach the sensor a few centimeters downstream without recombination, as reported elsewhere.[18, 40, 43]

Considering future applications, the nanocalorimeter detection threshold can be defined here as the radical flux associated with a temperature signal rise equal to three-fold the noise level (signal-to-noise ratio = 3). The maximal recorded peak-to-peak amplitude of the temperature noise oscillations is 0.5 degrees (see inset in Figure 2 b), which introduces a temperature detection limit of 1.5 K. The substitution in Eq. 3 of this temperature resolution threshold yields a hydrogen radicals flux reliable detection limit of ~$2 \cdot 10^{20}$ $m^{-2}s^{-1}$ and a corresponding radical density of ca. $4 \cdot 10^{17}$ m^{-3}. These values show that even unoptimized nanocalorimeters used in his study are as sensitive as the advanced calorimetric probes previously reported but have significantly shorter response times. [22, 23] Since plasma-induced electronic noise was found to be the major reason for the signal uncertainty, further sensitivity optimizations will be achieved by implementing corresponding filters and lock-in techniques. Apparently, the reported sensitivity numbers are still well below the optical actinometry detection limits.[42] However, one has to emphasize that nanocalorimetry measurements can still be performed under remote plasma conditions where optical emission signals often fade below the detection limits.

Finally, since the product of the nanocalorimeter's flux sensitivity and response time is approaching the 10^{19} m^{-2} value, nanocalorimeters could potentially be used to track monolayer-level plasma-assisted deposition or etching processes.

IV. CONCLUSIONS AND OUTLOOK

Compared to the more common radicals' sensors of mass or heat exchange, like etch sensors and standard thermocouple or thermopile-based calorimetric probes, the microfabricated nanocalorimeter excels in sensitivity and response time. In this study, we demonstrate a sensor response time of 40 ms thanks to the drastically reduced thermal mass of the (Au, Al_2O_3)/SiN

membrane/Pt layer stack. Such response time is significantly lower than the seconds to tens of seconds response time of the typical plasma calorimetric sensors. Moreover, the response time reported here is mainly determined by radicals' diffusion time inside the plasma source assembly after plasma ON/OFF onsets, while the sensors themselves are capable of resolving 0.1 ms spread events[31]. This makes nanocalorimeters perspective for monitoring fast transients routinely employed in plasma-assisted pulsed processes such as atomic layer deposition/etching (ALD/ALE). In the present work, nanocalorimetry has proven efficient as a technique complementary to OES or optical actinometry, thanks to its capability to quantify H radical fluxes and densities under remote plasma conditions where optical emission becomes negligible. In addition, the potential to reduce the size of the individual sensors to micron and even submicron level, well below the molecular mean free path (ca. 1 mm at 10 Pa, 300 K in hydrogen) and mass-produce them as 2D and 3D arrays, paves the way to design novel "noninvasive" plasma probing platforms that can be used for sensing and imaging of plasma parameters in 2D and 3D. Moreover, sensitizing individual nano-sensors with different catalytic materials within multi-sensor arrays opens unprecedented opportunities in multidimensional plasma parameter recognition and machine learning[44]. Ultimately, the envisaged integration of scanning nanocalorimeters with other optical and electrical metrologies (e.g., QMC, OES, RFEA) on a single-chip platform offers a significant advancement in plasma process monitoring for the semiconductor industry.

ACKNOWLEDGMENTS AND DISCLAIMERS

This work was performed with funding from the CHIPS Metrology Program, part of CHIPS for America, National Institute of Standards and Technology, U.S. Department of Commerce. CHIPS

for America has financially supported this work through the “Multiscale Modeling and Validation of Semiconductor Materials and Devices project”. Any mention of commercial products in this article is for information only; it does not imply recommendation or endorsement by NIST.

AUTHOR DECLARATIONS

The authors have no conflicts to disclose.

Author Contributions

J. Trey Diulus: Data curation (lead): Formal analysis (equal); Investigation (lead); Writing – review & editing (supporting). Carles Corbella: Data analysis (equal); Investigation (supporting); Writing – original draft (lead); Writing – review & editing (equal). Feng Yi: Device fabrication (lead); Formal analysis (supporting); Investigation (equal); Writing – review & editing (supporting).

David LaVan, Berc Kalanyan, Mark McLean, Lakshmi Ravi Narayan, William A. Osborn, James E. Maslar: Device fabrication (supporting); Formal analysis (supporting); Investigation (supporting); Writing – review & editing (supporting). Andrei Kolmakov: Conceptualization (lead); Formal analysis (equal); Investigation (supporting); Supervision (lead); Writing –review & editing (lead).

DATA AVAILABILITY

The data that support the findings of this study are available from the corresponding author upon reasonable request.

REFERENCES

1. G. S. Oehrlein, S. M. Brandstadter, R. L. Bruce, J. P. Chang, J. C. DeMott, V. M. Donnelly, R. Dussart, A. Fischer, R. A. Gottscho and S. Hamaguchi, Journal of Vacuum Science Technology B **42** (4) (2024).
2. D. B. Graves, C. B. Labelle, M. J. Kushner, E. S. Aydil, V. M. Donnelly, J. P. Chang, P. Mayer, L. Overzet, S. Shannon and S. Rauf, Journal of Vacuum Science Technology B **42** (4) (2024).

3. P. Hargis Jr, K. Greenberg, P. Miller, J. Gerardo, J. Torczynski, M. Riley, G. Hebner, J. Roberts, J. K. Olthoff and J. Whetstone, Review of Scientific Instruments **65** (1), 140-154 (1994).
4. A. von Keudell and C. Corbella, Journal of Vacuum Science Technology A **35** (5) (2017).

5. U. Fantz, Plasma sources science technology **15** (4), S137 (2006).

6. W. J. Tango, J. K. Link and R. N. Zare, The Journal of Chemical Physics **49** (10), 4264-4268 (1968).
7. N. Britun, T. Minea, S. Konstantinidis and R. Snyders, Journal of Physics D: Applied Physics **47** (22), 224001 (2014).
8. J. Benedikt, A. Hecimovic, D. Ellerweg and A. Von Keudell, Journal of Physics D: Applied Physics **45** (40), 403001 (2012).
9. J. Benedikt, H. Kersten and A. Piel, Plasma Sources Science **30** (3), 033001 (2021).
10. M. Ohring, Materials Science of Thin Films, 559-640 (2002).
11. C. Corbella, S. Grosse-Kreul, O. Kreiter, T. de los Arcos, J. Benedikt and A. von Keudell, Review of Scientific Instruments **84** (10) (2013).
12. B. Biskup, C. Maszl, W. Breilmann, J. Held, M. Böke, J. Benedikt and A. Von Keudell, Journal of Physics D: Applied Physics **51** (11), 115201 (2018).
13. K. Arts, J. Deijkers, T. Faraz, R. Puurunen, W. M. Kessels and H. C. Knoops, Applied Physics Letters **117** (3) (2020).
14. D. van Leuken, C. de Meijere, R. Van der Horst, V. Banine, E. Osorio and J. Beckers, Review of Scientific Instruments **92** (6) (2021).
15. M. Mozetic, Surface Coatings Technology **201** (9-11), 4837-4842 (2007).
16. M. Stahl, T. Trottenberg and H. Kersten, Review of Scientific Instruments **81** (2) (2010).
17. M. Mozetič and A. Zalar, Applied surface science **158** (3-4), 263-267 (2000).
18. R. Grubbs and S. George, Journal of Vacuum Science Technology A **24** (3), 486-496 (2006).
19. S. Bornholdt and H. Kersten, The European Physical Journal D **67**, 1-11 (2013).
20. D. Qerimi, G. Panici, A. Jain, D. Jacobson and D. N. Ruzic, Journal of Vacuum Science Technology A **39** (2) (2021).
21. J. F. Velthuis, A. Storm, M. van Kampen, R. van der Horst and H. B. Profijt, Journal of Vacuum Science & Technology A **37** (6) (2019).
22. M. Mozetic, A. Vesel, A. Drenik, I. Poberaj and D. Babic, Journal of nuclear materials **363**, 1457-1460 (2007).
23. D. Qerimi, I. Shchelkanov, G. Panici, A. Jain, J. Wagner and D. N. Ruzic, Journal of Vacuum Science Technology A **39** (2) (2021).

24. J. A. Thornton, Thin solid films **54** (1), 23-31 (1978).
25. M. Mozetič, M. Kveder, M. Drobnič, A. Paulin and A. Zalar, Vacuum **45** (10-11), 1095-1097 (1994).
26. M. Mozetič, M. Drobnič, A. Pregelj and K. Zupan, Vacuum **47** (6-8), 943-945 (1996).
27. C. Schick and V. Mathot, *Fast scanning calorimetry*. (Springer, 2016).
28. R. E. Cavicchi, G. Poirier, N. Tea, M. Afridi, D. Berning, A. Hefner, J. Suehle, M. Gaitan, S. Semancik and C. Montgomery, Sensors and Actuators B: Chemical **97** (1), 22-30 (2004).
29. D. Denlinger, E. Abarra, K. Allen, P. Rooney, M. Messer, S. Watson and F. Hellman, Review of Scientific Instruments **65** (4), 946-959 (1994).
30. S. Lai, G. Ramanath, L. Allen, P. Infante and Z. Ma, Applied physics letters **67** (9), 1229-1231 (1995).

31. J. B. DeLisio, F. Yi, D. A. LaVan and M. R. Zachariah, The Journal of Physical Chemistry C **121** (5), 2771-2777 (2017).
32. S. Lai, J. Carlsson and L. Allen, Applied Physics Letters **72** (9), 1098-1100 (1998).
33. F. Yi and D. A. LaVan, Applied Physics Reviews **6** (3) (2019).
34. Y. Gao, B. Zhao, J. J. Vlassak and C. Schick, Progress in Materials Science **120**, 100819 (2021).
35. F. Yi, M. D. Grapes and D. A. LaVan, Journal of Research of the National Institute of Standards Technology **124**, 1 (2019).
36. B. Lavrov, M. Osiac, A. Pipa and J. Röpcke, Plasma Sources Science Technology **12** (4), 576 (2003).
37. B. Lavrov, A. Pipa, J. Röpcke and Technology, Plasma Sources Science **15** (1), 135 (2006).
38. I. Mendez, F. J. Gordillo-Vázquez, V. J. Herrero and I. Tanarro, The Journal of Physical Chemistry A **110** (18), 6060-6066 (2006).
39. B. J. Wood and H. Wise, The Journal of Chemical Physics **29** (6), 1416-1417 (1958).
40. A. S. Stodolna, S. Ramankutty, M. Blauw, T. de Jonge, A. J. Storm and J. Velthuis, Journal of Vacuum Science Technology A **42** (5) (2024).
41. B. J. Wood and H. Wise, The Journal of Physical Chemistry **65** (11), 1976-1983 (1961).
42. N. Škoro, N. Puač, S. Lazović, U. Cvelbar, G. Kokkoris and E. Gogolides, Journal of Physics D: Applied Physics **46** (47), 475206 (2013).
43. M. Mozetiča and M. Drobnič, Vacuum **50** (3-4), 319-322 (1998).
44. R. Gutierrez-Osuna, IEEE Sensors journal **2** (3), 189-202 (2002).